DOI: 10.1111/cgf.14055
Eurographics Symposium on Rendering 2020
C. Dachsbacher and M. Pharr
(Guest Editors)

Volume 39 (2020), Number 4

Practical Measurement and Reconstruction of Spectral Skin Reflectance

Y. Gitlina[1] G. C. Guarnera[2,3] D. S. Dhillon[1,4] J. Hansen[5] A. Lattas[1] D. Pai[5] A. Ghosh[1]

[1]Imperial College London [2]NTNU [3]University of York [4]Clemson University [5]UBC

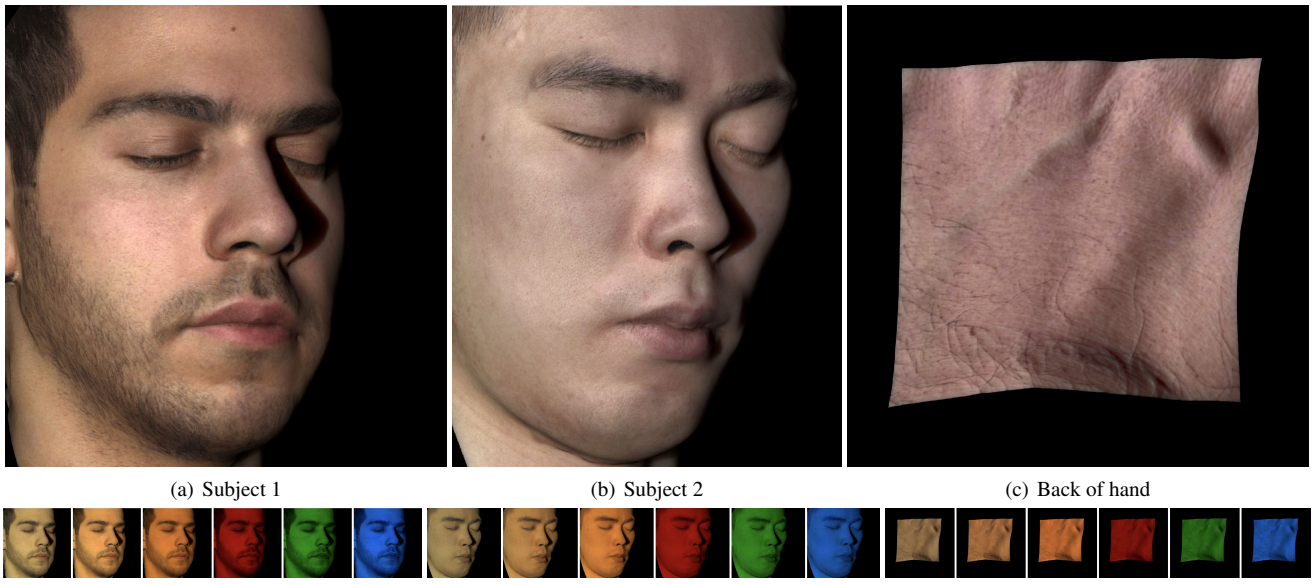

(a) Subject 1 (b) Subject 2 (c) Back of hand

Figure 1: *Renderings of acquired faces (a, b) and a patch of skin (back of hand) using our proposed practical spectral measurement and reconstruction approaches. Spatially-varying spectral skin parameters for subject 1 (a, Mediterranean skin type), and subject 2 (b, Asian skin type) acquired using an LED sphere, while the back of the hand (c, South Asian skin type) has been acquired using a hand-held dermatological skin measurement device (Antera3D). Top-row: Renderings (using PBRT) with a spectral BSSRDF under a point source illumination with broadband D65 spectrum. Bottom-row: Diffuse-only renderings under six different LED spectras (W57, W40, W27, Red, Green, Blue).*

Abstract

We present two practical methods for measurement of spectral skin reflectance suited for live subjects, and drive a spectral BSSRDF model with appropriate complexity to match skin appearance in photographs, including human faces. Our primary measurement method employs illuminating a subject with two complementary uniform spectral illumination conditions using a multispectral LED sphere to estimate spatially varying parameters of chromophore concentrations including melanin and hemoglobin concentration, melanin blend-type fraction, and epidermal hemoglobin fraction. We demonstrate that our proposed complementary measurements enable higher-quality estimate of chromophores than those obtained using standard broadband illumination, while being suitable for integration with multiview facial capture using regular color cameras. Besides novel optimal measurements under controlled illumination, we also demonstrate how to adapt practical skin patch measurements using a hand-held dermatological skin measurement device, a Miravex Antera 3D camera, for skin appearance reconstruction and rendering. Furthermore, we introduce a novel approach for parameter estimation given the measurements using neural networks which is significantly faster than a lookup table search and avoids parameter quantization. We demonstrate high quality matches of skin appearance with photographs for a variety of skin types with our proposed practical measurement procedures, including photorealistic spectral reproduction and renderings of facial appearance.

CCS Concepts

• ***Computing methodologies*** → ***Reflectance modeling; Computational photography;***

1. Introduction

Accurate modeling and rendering of human skin appearance has been a long standing goal in computer graphics. Of particular importance has been the realistic modeling and rendering of layered reflectance and subsurface scattering in skin for which researchers have proposed various diffusion-based models [JMLH01, DJ05] and measurement techniques [WMP*06, GHP*08]. Recently, various bio-physical models of skin appearance have been proposed, mostly based on the spectral distribution of chromophores in the epidermal and deeper dermal layers of skin [DJ06, DWd*08, CBKM15, IGAJG15]. However, measurement of the spectral parameters of absorption and scattering of light in skin for such bio-phyisical models has been a challenge in computer graphics. Previous works have either borrowed parameters from tissue-optics literature [Tuc07], or employed extensive multispectral imaging for inverse rendering detailed spatially varying parameters for a patch of skin [DWd*08]. Closest to our approach, Jimenez et al. [JSB*10] employed observations under uniform broadband illumination to estimate two dominant parameters of melanin and hemoglobin concentrations for driving a qualitative appearance model for facial animation.

In this work, we propose a novel practical spectral skin measurement approach (using an LED sphere) that, in conjunction with driving the spectral skin BSSRDF of [JSB*10] with appropriate model complexity, is suitable for facial capture of live subjects with realistic spectral appearance reproduction (Section 4). We demonstrate that the proposed model complexity involving four parameters (melanin C_m and hemoglobin C_h concentration, melanin blend-type fraction β_m, and epidermal hemoglobin C_{he} fraction) is required to match subject appearance in photographs, which may not be possible using a reduced model with just two free parameters (melanin and hemoglobin), and our proposed measurement protocol combining two complementary broad and narrow-band spectral illumination conditions provides higher quality estimates of spectral parameters than those obtained using just broadband illumination. Additionally, we demonstrate how to acquire ideal broadband and narrowband illumination measurements for parameter estimation within the practical constraints of LED illuminants and regular color cameras. Thus, as our *primary* contribution, we propose a minimal measurement and modeling complexity for data-driven reproduction of spatially varying spectral appearance of skin, including human faces.

We also demonstrate how practical measurements with a hand-held off-the-shelf skin measurement device designed for dermatological applications (a Miravex Antera3D camera) can be adapted for realistic skin appearance reproduction and rendering (Section 5). Here, we demonstrate how to appropriately transform the output pigmentation and redness maps produced by the device into melanin and hemoglobin concentrations respectively, and augment them with additional model parameters (β_m and C_{he}) which are not provided by the device. Additionally, we demonstrate how neural networks can be employed for faster, improved parameter estimation given our measurements (Section 6). Finally, we demonstrate realistic rendering of subsurface scattering with our estimated parameters (in PBRT) using spatially-varying diffusion profiles (Section 7), achieving renderings of human faces using a biophysically based spectral BSSRDF that are, for the *first* time, comparable to photographs (see Figure 1).

To summarize, our central high-level contributions in this work are as follows:

- Practical measurement of spectral skin reflectance suitable for facial capture in conjunction with appropriate model complexity of spectral BSSRDF for matching skin appearance in photographs.
- Adaption and augmentation of chromophore maps obtained from a hand-held dermatological skin measurement device for realistic rendering.
- Novel estimation of parameters from our measurements using neural networks, which is significantly faster than a look-up table search along with reduced quantization.

We additionally propose the following practical contributions for spectral measurements with a color camera:

- An optimization procedure for combining a set of broad- and narrow-band LED illuminants to construct a metamer for desired D65 illumination.
- Novel indirect measurement of narrow-band LED response that enables higher quality measurement with sharper spectral isolation than direct measurement with a color camera.
- A genetic programming algorithm for estimation of unknown illumination spectra from a single colorchart observation.

2. Previous Work

We restrict the discussion here to the most relevant previous work in graphics and vision on modeling and measurement of spectral skin appearance. We refer the interested reader to recent surveys for a broader review of skin [INN07] and facial appearance [WLL*09, KRP*15] modeling.

Bio-physical Skin Appearance Modeling: The seminal work of Jensen et al. [JMLH01] first introduced efficient BSSRDF modeling for highly translucent materials in computer graphics using dipole diffusion. Donner & Jensen [DJ05] extended this work with the introduction of multi-layered diffusion using the multipole model for modeling layered scattering in human skin, borrowing RGB scattering and absorption parameters for the various layers of skin from tissue optics literature [Tuc07]. They subsequently proposed a diffusion based spectral skin BSSRDF model [DJ06] that was well suited for artistic modeling of skin appearance using intiutive parameters which directly control skin coloration. Importantly, their model simplified the skin layers into two primary layers: epidermis and dermis, with parameters corresponding to respective chromophore concentrations. This spectral BSSRDF model has been the basis of significant follow-up work: Donner et al. [DWd*08] further extended the model with a more detailed set of parameters including epidermal hemoglobin fraction and inter-layer absorption, and simulated truly heterogenous subsurface scattering in skin using a path-tracing framework. Jimenez et al. [JSB*10] simplified the detailed model of [DWd*08] to make it suitable for practical measurement and modeling of qualtiative change in skin appearance during facial performance/animation. We build upon the work of Jimenez et al. which has a similar focus on a practical technique. However, their proposed reduced model for facial animation only has the two dominant parameters of melanin C_m and hemoglobin C_h concentration as free parameters which we show to be insufficient for matching the spatial variation of facial skin. Furthermore, Jimenez et al. focus

on modeling local changes in albedo color due to blood flow, while employing a fixed translucency parameter over the entire face in order to support real-time rendering with screen-space subsurface scattering [JSG09]. Besides reconstructing the albedo color with higher accuracy using their extended model with four parameters, we also render heterogeneous subsurface scattering in skin using spatially varying diffusion profiles which are precomputed from the estimated parameters. Importantly, we do *not* employ a modulation texture for rendering, but reconstruct skin color variation through the subsurface scattering process.

There have been a few alternate notable works in computer graphics on detailed bio-physical modeling of skin including the BioSpec [KB04] and the more recent Hyperspectral [CBKM15] models of skin appearance, as well as recently proposed bio-physical model of skin ageing [IGAJG15]. While highly accurate in the extent of bio-physical simulation of skin appearance due to various physiological factors, these models are rather complex for inverse rendering for driving these models from measurements. Hence, in this work we focus on a simpler diffusion-based spectral model of skin for estimating model parameters from measurements.

Spectral Skin Appearance Measurement: While there has been significant work in graphics and vision on standard RGB measurement of skin reflectance, there have been fewer works focused on spectral measurement of skin. Tsumura et al. [TOS*03] proposed applying independent component analysis on regular facial images to estimate melanin and hemoglobin maps for physiologically motivated image-based editing effects. Donner et al. [DWd*08] were the first to carry out extensive multispectral imaging of skin patches for driving their detailed heterogeneous model of skin reflectance. Their setup involved a broadband flash incident on a patch of skin while a camera equipped with a spectral filter wheel records nine different chosen narrow spectral bands of reflectance. The acquired spectral measurements are thereafter employed in an inverse rendering pipeline for model parameter estimation. While enabling highly accurate estimation of the detailed spectral parameters of skin reflectance, the approach is limited to imaging a skin patch and is not well suited for facial acquisition. Hence, Jimenez et al. [JSB*10] employed just a single measurement with a color camera under uniform broadband (flash) illumination to estimate spatially varying parameters of melanin and hemoglobin concentrations over a face, and more specifically local changes in hemoglobin concentrations during facial performance, using the measurement procedure of [CCH99]. A similar measurement procedure utilizing broadband LED illumination has also been employed by [AS17] to estimate melanin and hemoglobin concentrations over a face for building a biophysical morphable model of skin appearance. Compared to these works that employ just broadband illumination measurements, we demonstrate that spectral parameter estimation of skin can be improved using a combination of *two* complimentary spectral measurements involving both broadband and narrow band (blue) illumination, while still being well suited for practical facial capture. We also demonstrate how to acquire ideal broad- and narrow-band measurements for skin with a regular color camera and LED illumination.

Also related to our work is that of LeGendre et al. [LYL*16] and Wenger et al. [WHD03] who employ multispectral LED illumination for improving image-based lighting reproduction. While the focus of these works is on matching the appearance of a subject under a specific lighting condition, our focus is on spectral parameter estimation of skin in order to reproduce its appearance under any desired spectral illumination. Our spectral acquisition procedure with LED illumination has some similarity to the multiplexed illumination approach proposed by Park et al. [PLGN07]. However, Park et al. focused on optimal spectral estimation of general scene reflectance using an optimization procedure based on a color chart, whereas we specifically design our two complementary illumination conditions based on the reponse of a spectral skin BSSRDF model and hence achieve better matching of skin appearance under different spectral lighting conditions. Our proposed choice of the additional narrow band measurement is also supported by a previous study on optimal spectral filter selection for skin by Preece & Claridge [PC04]. However, instead of direct measurement of skin under narrow band (blue LED) illumination which produces some colors outside the gamut of a regular color camera, we directly only measure skin response to a mixture of narrowband and broadband illumination, and afterwards *computationally* separate the desired narrowband response from the mixture. We note that this process bears some conceptual similarity to sensor sharpening approaches employed for color constancy [BCF01]. We demonstrate higher quality *descattered* measurement with this proposed indirect measurement of skin response to narrowband illumination. Besides optimal spectral measurements for facial acquisition, we also demonstrate how to adapt practical skin patch measurements obtained with a hand-held dermatological imaging device for photorealistic skin appearance reconstruction and rendering.

3. Spectral BSSRDF Model Complexity

We aim to drive a spectral skin BSSRDF model with practical measurements and hence prefer a model with an appropriately minimal complexity to simplify measurements while simultaneously having sufficient complexity to match the observed spatial variation in skin, particularly facial appearance. In this respect, we aim for a data-driven modeling of skin and facial appearance rather than striving for strict bio-physical accuracy of the estimated parameters. We choose the model of Jimenez et al. [JSB*10], originally proposed for facial measurements, as the starting point for our work. The model includes the following four parameters: melanin concentration (C_m) in epidermis, melanin blend-type fraction β_m (blend between eumelanin and pheumelanin), and hemoglobin concentration (C_h) in dermis, and epidermis (C_{he}), respectively (please see Supplemental material for details). However, unlike Jimenez et al., we have emperically found that all four parameters in the model need to be varied over the skin surface in order to closely match the appearance of real skin. Variation in β_m is particularly useful for reconstructing facial appearance variation due to facial hair and around eyelids, while a higher fraction of epidermal hemoglobin C_{he} is necessary to match the very reddish areas of a face such as the lips and cheeks. Hence, we allow β_m to vary between $0.0 - 1.0$, and C_{he} to vary between $0.0 - 0.6$. We also set epidermal thickness d to $0.33mm$ instead of $0.25mm$ suggested in previous work in order to better match the appearance of subjects with the above spectral model.

This leads to a 4D spectral skin appearance model. In practice,

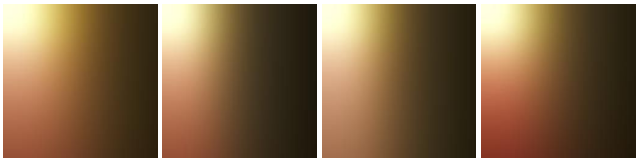

(a) $\beta_m = 0.0$ (b) $\beta_m = 1.0$ (c) $C_{he} = 0.1$ (d) $C_{he} = 0.6$

Figure 2: *Spectral skin reflectance model variation due to β_m (a, b), and C_{he} (c, d) parameters, respectively. Individual 2D LUTs represent variation due to the dominant parameters C_m (x-axis) and C_h (y-axis).*

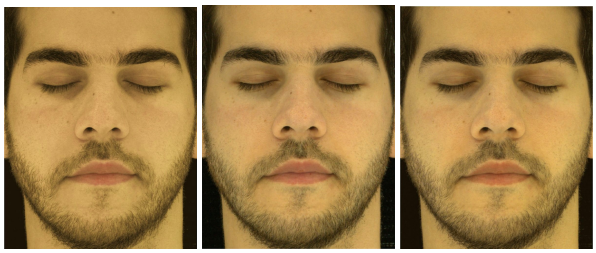

(a) 2D model (b) Photograph (c) 4D model

Figure 3: *Comparison of a facial photograph under uniform broadband (W57 cool white LED) illumination (b) to reconstructions using the reduced 2D spectral model of Jimenez et al. [JSB*10] (a), and using the complete 4D model (c) which enables a much closer match to the photograph.*

in order to restrict the search space of the various parameters for model-fitting, we employ very coarse discretization for β_m (10 bins) and C_{he} (4 bins) parameters which have a more subtle effect on the overall appearance, while employing a large number of bins to model the dominant variation in C_m and C_h. Figure 2 shows the variation due to the two dominant parameters as a 2D LUT, while showing more subtle variation due to the β_m parameter across (a, b) (for fixed $C_{he} = 0.25$), and variation due to the C_{he} fraction parameter across (c, d) (for fixed $\beta_m = 0.5$).

Figure 3 shows comparison of a facial photograph under uniform broadbad illumination, and its reconstruction using the reduced 2D model employed by Jimenez et al. [JSB*10] with only two free parameters (C_m and C_h) (a), and reconstruction using the complete 4D model with two additional free parameter (β_m, and C_{he}) (c). As can be seen, the 4D model complexity allows a closer match to the spatially varying appearance of skin in the photograph. We provide additional comparisons in the Supplemental material.

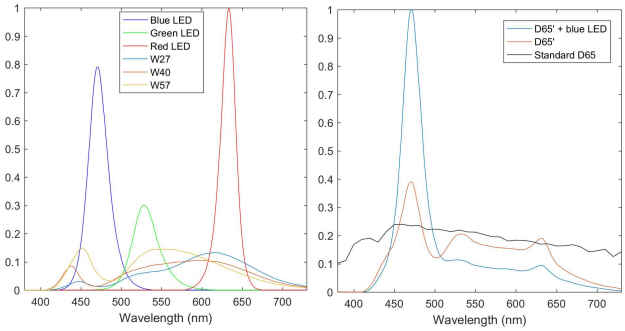

(a) (b)

Figure 4: *(a) Spectral power distributions of the 6 different LEDs installed on the multispectral LED sphere. (b) Spectra of D65′ and D65′ + blue illumination, jointly used to isolate the blue response (Section 4.2).*

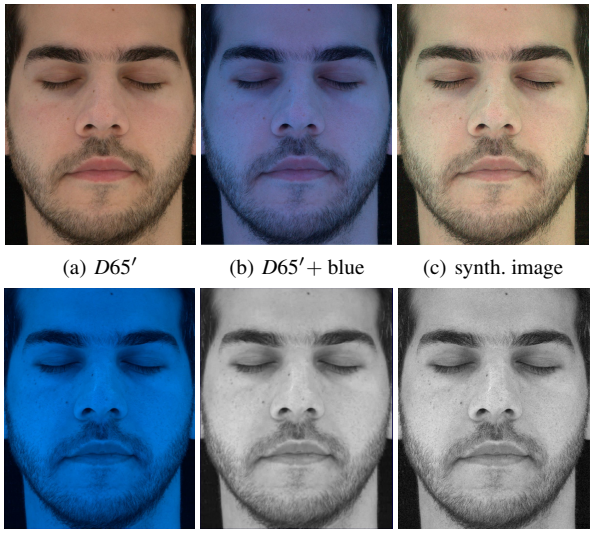

(a) $D65'$ (b) $D65'$+ blue (c) synth. image

(d) direct blue illum. (e) direct blue isol. (f) synth. blue isol.

Figure 5: *Proposed practical spectral measurements of skin reflectance (a, b). (a) Broadband D65 metamer (D65′) illumination. (b) Mix of D65′+ blue LED illumination. (c) Synthesized reponse to pure blue LED illumination, and its isolated blue channel data (f) employed for parameter estimation. (d) Direct measurement of skin response to blue illumination, and its isolated blue channel data (e).*

4. Practical Spectral Acquisition for Faces

We now present our practical measurement protocol for robustly estimating the four parameters of the BSSRDF model with a minimal set of measurements suitable for facial capture. We employ a multispectral LED sphere equipped with a combination of narrow band Red, Green, and Blue LEDs, and three types of broad band LEDs (warm 2700K, neutral 4000K, and cool 5700K which we refer to as W27, W40, and W57 respectively), and 9 color DSLR cameras (Canon 800D) for multiview acquisition of a subject. The LEDs on the sphere are all cross-polarized w.r.t. the cameras, allowing specular cancellation according to the method of [GFT*11]. We also measured the individual spectral distributions of our illuminants using a spectrometer (Sekonic SpectroMaster C700) placed at the center of the LED sphere (see Fig. 4, a). With this setup, we simultaneously record the diffuse reflectance response of a subject from multiple viewpoints under specific uniform spectral illumination conditions as described next.

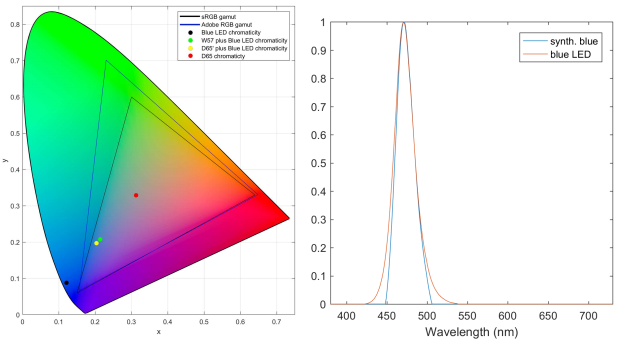

(a) (b)

Figure 6: *(a) The chromaticity of the narrow band blue LED lies outside both the sRGB ITU-R BT.709 and Adobe RGB colour spaces. Mixing the narrow band blue LED with a broadband illumination (D65′ or W57) reports the chromaticity of the illumination within both gamuts. (b) Additional advantage is that the spectrum of the synthesized blue is narrower than the actual blue LED, contributing to sharp details correlated with melanin concentration.*

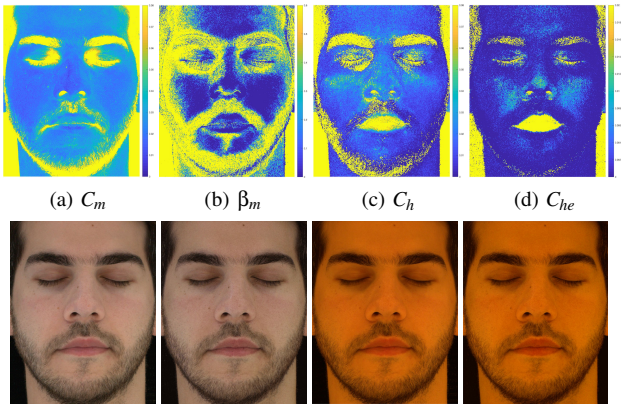

(a) C_m (b) β_m (c) C_h (d) C_{he}

(e) $D65'$ photo (f) $D65'$ recon. (g) $W27$ photo (h) $W27$ recon.

Figure 7: *Estimated spectral parameters for subject's face (top-row), and comparison of photographs with reconstructions under D65 metamer broadband illumination (e, f), and warmer W27 LED illumination not employed for parameter estimation (g, h).*

4.1. Measurement Protocol

With this setup, when we restricted ourselves to a single observation (as a baseline), we found the best individual LED illumination on our LED sphere for estimating model parameters to be uniform W57 (cool white LED) illumination (see Figure 3, b). Here, W57 illumination provided the highest color contrast in the skin reflectance for parameter estimation using CIELAB space color matching given a pre-computed 4D look-up table for the skin model under W57 illumination (more details in Supplemental material). Our choice of W57 broadband illumination is also supported by the study of Preece & Claridge [PC04] who found a peak around 560*nm* to be useful for measurement of hemoglobin concentration, and a peak around 485*nm* to be useful for measurement of melanin. Consistent with this study, we found improved parameter estimation when using *two* complementary spectral illumination conditions: a combination of broad band + narrow band blue LED illumination (480*nm* peak response). The premise here is that the blue illumination primarily only excites epidermal reflectance [PC04], while broadband illumination excites both epidermal and dermal reflectance. The response to narrow-band blue illumination exibits sharper skin texture (melanin response) due to reduced scattering of the wavelength compared to broadband illumination. This enables us to estimate sharper *descattered* parameter maps when jointly employing the two complementary illumination conditions for LUT search. Furthermore, instead of making direct measurements under W57 and blue LED illumination respectively, we instead employ the following procedure:

Ideal broadband measurement: Given the 6 types of LEDs in our LED sphere, we instead create a more ideal broadband illumination by computing a weighted combination of all 6 LEDs to create a D65 metamer spectra ($D65'$) which we instead employ for our broadband measurements. We notice an even higher contrast in skin color, particularly coloration due to skin pigmentation and redness, under the D65 metamer illumination and we make the observation that D65 spectrum (blue dominant) balances the somewhat skewed red-dominant reflectance spectrum of human skin (see Supplemental material). This is consistent with studies on the human visual system [CXW19] where D65 spectrum has been reported to be most desirable for discerning differences in skin color. Note that true D65 illumination is not possible with the LEDs on our LED sphere. Instead, the D65 metamer is created to be an approximation of the ideal D65 spectra achieved by the available LEDs such that it minizes the color difference between the 24 color patches measured on an Xrite color chart vs the reference 24 colors on an ideal colorchart in sRGB color space (which assumes ideal D65 spectrum). Our computed metamer spectrum can be seen in comparison to the ideal D65 spectrum in Fig. 4(b). We provide more details on how to compute the D65 metamer in Appendix A.

Narrow-band measurement: Directly recording the reflectance response of a subject under blue LED illumination unfortunately results in some colors being outside the gamut of most off-the-shelf color cameras, which typically work in the sRGB and Adobe RGB colour spaces, with the chromaticity of the narrow band being noticeably outside both colour spaces (Figure 6(a)). This results in suboptimal narrow-band measurements. Instead, we propose a novel procedure to overcome this gamut limitation of regular color cameras by instead recording a mix of broadband and blue LED illumination during measurement, and given another measurement under uniform broadband illumination, we can then *computationally* isolate the narrow band response to just blue LED illumination afterwards as described next.

4.2. Isolation of Blue Response

We propose an indirect scheme in order to measure skin response under blue LED illumination. We capture two photographs of a subject, the first one under broadband lighting (I_W) and the second one under broadand plus blue LED (I_{W+nb}). We then separately apply to both the images a Chromatic Adaptation Transform (CAT) (defined in Appendix B), to predict colours appearance under D65

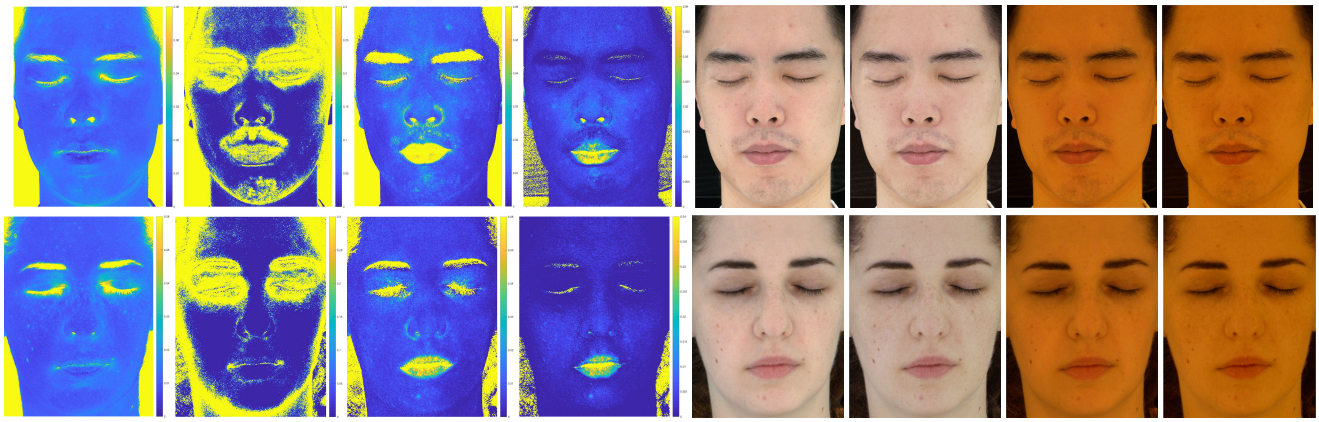

(a) C_m (b) β_m (c) C_h (d) C_{he} (e) $D65'$ photo (f) $D65'$ recon. (g) $W27$ photo (h) $W27$ recon.

Figure 8: *Estimated spectral parameters for faces of two subjects with different skin types, and comparison of photographs with reconstructions under different types of broadband illumination. Measurement using $D65'$ for broadband illumination.*

lighting and within the sRGB gamut, and computationally recover the desired narrow band response I_{nb} as follows:

$$I_{nb} = \delta \times (CAT\,(I_{W+nb}) - CAT\,(I_W)\,/\delta), \quad (1)$$

where the factor δ accounts for the difference in intensities of the LEDs in the two conditions.

In our case, we preferably employ D65 metamer illumination for the broadband measurement ($I_W = I_{D65'}$) which greatly simplifies it's CAT transform to identity matrix. However, the transform is general and can be employed with any broadband illumination (e.g., $W = W57$ cool white LED) for computing the spectral isolation as per Equation 1. The above scheme offers an additional advantage of actually measuring the skin response under a slightly narrower band than the one offered directly by blue LED (Figure 6(b)), further contributing to sharper details in the measurement.

The capture process can be visually seen in Figure 5 where the response of a subject's face to our proposed two complimentary uniform spectral illumination conditions (a, b) are shown in the top row. Afterwards, we can computationally synthesize the response to pure blue illumination as shown in (c). Note that only the blue channel of this synthesized image is relevant for our analysis, while the red and green channels of (c) are residuals of CAT transform after white-balancing, which is why they are ignored. The isolated blue measurement from the synthesized image can be seen in grayscale in (f) showing skin texture and blemishes in sharp detail which is very correlated with skin melanin concentration. Figure 5(d) instead shows the subject's direct response to pure blue LED illumination as recorded by the color camera, where some spatial details of the skin texture are lost in the isolated blue component (e) of image (d). We include similar example images for a subject acquired using W57 LED for the broadband condition in the Supplemental material. Note that our preferred choice of broadband illumination ($D65'$) and indirect measurement of the narrow-band illumination also has a practical advantage of employing all types of LED illuminants in our measurement setup, thereby creating much brighter lighting conditions for faster higher quality measurements compared to when employing a single type of LED.

4.3. Results

With the measurement protocol described in Section 4.1, we do a joint look-up table search for best matching color values (in CIELAB space) under simulated D65 metamer illumination (Figure 5, a), and best matching synthesized blue channel response under simulated blue LED illumination (Figure 5, f). Figure 7 (top-row) presents the various parameter maps (C_m, β_m, C_h, C_{he}) estimated for a subject's face using the above acquisition and fitting procedure. Here, we are visualizing the total C_{he} fraction and not as a fraction of C_h. Figure 7 (bottom-row) presents comparisons of photographs of the subject and our reconstruction with the estimated praramters under D65 metamer illumination and a warmer spectral illumination condition (W27) which was not employed in parameter estimation. A similar comparison under W57 illumination can be see in Figure 3.

Figure 8 presents the estimated parameter maps using our proposed two complementary spectral measurements, and comparison of spectral reconstructions to photographs for two subjects with different skin types. These include a male subject with Asian skin type, and a Caucasian female subject with a pale skin type whose measurements we acquired using the D65 metamer ($D65'$) as the broadband illumination. As can be seen, the reconstructions are a close match to the photographs under different types of illumination spectrum. The estimated parameters maps not only well reconstruct the appearance of skin well under cooler illumination spectrum, they also appropriately predict the softening and blurring of the skin texture seen under the warmer W27 illumination. The Supplemental material includes an additional example of a Caucasian male subject whose measurement was acquired using the cool white LED (W57) as the broadband illumination, as well as results for a palm of a hand. We provide additional analysis in Section 7.

5. Practical Skin Measurements with Antera3D

The focus of the previous section was on practical spectral measurements of skin in a controlled setup suitable for facial capture. For more free-form measurement of skin, we employ a hand-held off-the-shelf device - Antera 3D® (Miravex Limited, Ireland), a camera

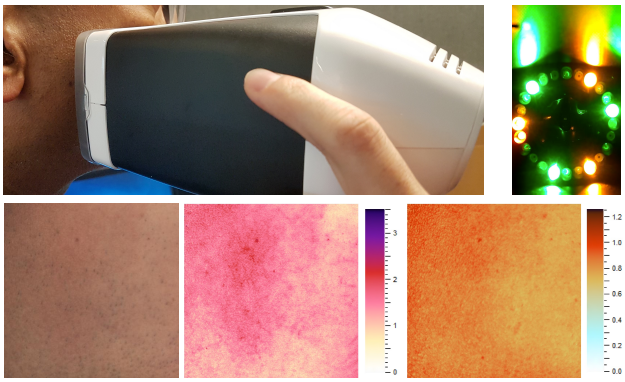

(a) Color map (b) Redness map (c) Pigmentation map

Figure 9: *Measurement of a subject's cheek with the Antera 3D® (top) and example of acquired chromophore maps (bottom). Photograph of the device's multi-LED illumination setup surrounding the camera lens (top-right).*

for image acquisition and corresponding software for analysis of single skin patches (56×56 mm^2). This is an instrument employed in dermatology: it has been compared with most commonly used devices in dermatological research and is reported to be robust, sensitive and precise for skin colour analysis [MFCN15, LWA*18]. For a single measurement, the camera is placed onto a skin patch without applying excessive pressure. The typical measurement procedure along with sample results for a cheek patch is shown in Figure 9. Any area of the human body can be captured in less than 2 seconds at a resolution of 0.1 mm. The acquisition procedure with the device is as follows: The device consists of a camera and various LEDs covering seven different spectral bands (narrow and broad band) in a single self-contained unit. During acquisition, the device illuminates the skin patch sequentially with its spectral LEDs from different angles. The obtained reflectance data are transformed by the vendor's proprietary software into skin absorption coefficients and used to quantify chromophore concentrations using mathematical correlation with known spectral absorption data of hemoglobin and melanin. The software provides spatially varying maps of these two chromophore concentrations as well as corresponding 3D surface geometry of the skin patch which is estimated using photometric stereo. The device also provides a color (albedo) map of the skin surface estimated using the acquisition process.

This is a good starting point for employing the data for spectral rendering of skin. However, the device does not capture *all* of the parameters we have identified as necessary for reproduction of skin appearance. Importantly, for the two parameters that are provided, the device provides chromophore concentrations in terms redness and pigmentation which do *not* directly map as C_m and C_h for the BSSRDF model. Hence, we have to undertake a number of steps in order to adapt the Antera measurements for driving the skin appearance model.

5.1. Parameter Remapping and Estimation

Given that Antera estimates only the two primary parameters (pigmentation and redness) related to melanin and hemoglobin concentration, in a first step we adapt these maps based on Jiminez et al.'s

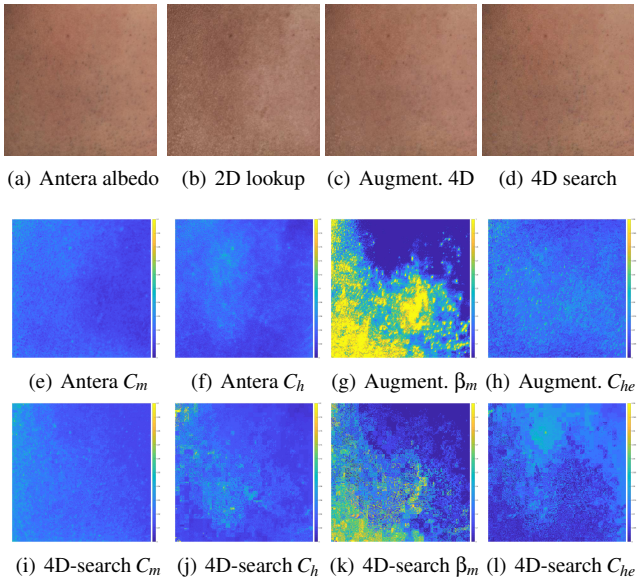

(a) Antera albedo (b) 2D lookup (c) Augment. 4D (d) 4D search

(e) Antera C_m (f) Antera C_h (g) Augment. β_m (h) Augment. C_{he}

(i) 4D-search C_m (j) 4D-search C_h (k) 4D-search β_m (l) 4D-search C_{he}

Figure 10: *Estimating skin patch parameters using Antera data. Parameters obtained by adapting and augmenting Antera's maps (center row) exhibit higher physiological correlation and lower noise than parameters estimated using a full 4D search based on the albedo (bottom-row). However, reconstruction with the latter approach is a closer match to the albedo map.*

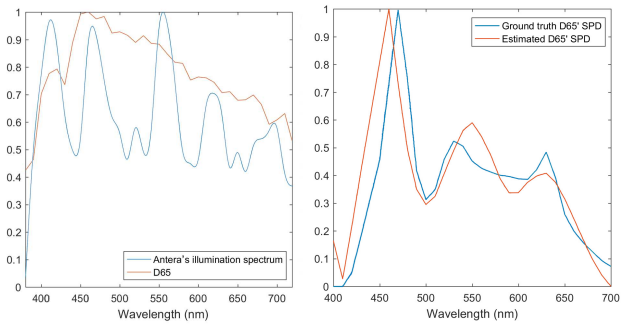

(a) Estimated spectrum (b) Validation

Figure 11: *(a) Spectrum of Antera's LEDs estimated using proposed genetic programming based optimization. (b) Validation of estimation procedure on D65′ spectrum achieved with the LED sphere.*

reduced 2D model of skin appearance. In order to do this, we employ the albedo map provided by Antera and estimate corresponding C_m and C_h for the Jimenez model using the same look-up table search procedure (in CIELAB space) described in the previous section. Given our best fit to the 2D model, we then scale antera's maps for pigmentation and redness in an appropriate manner to match the mean and variance of our estimated C_m and C_h parameters (using color space matching), and set these scaled pigmentation and redness maps as our final estimate of C_m and C_h for reconstruction. Figure 10 (b) shows reconstruction for the measured cheek patch using this 2D remapping procedure using the reduced Jimenez model.

Note that this above remapping step requires us to simulate a

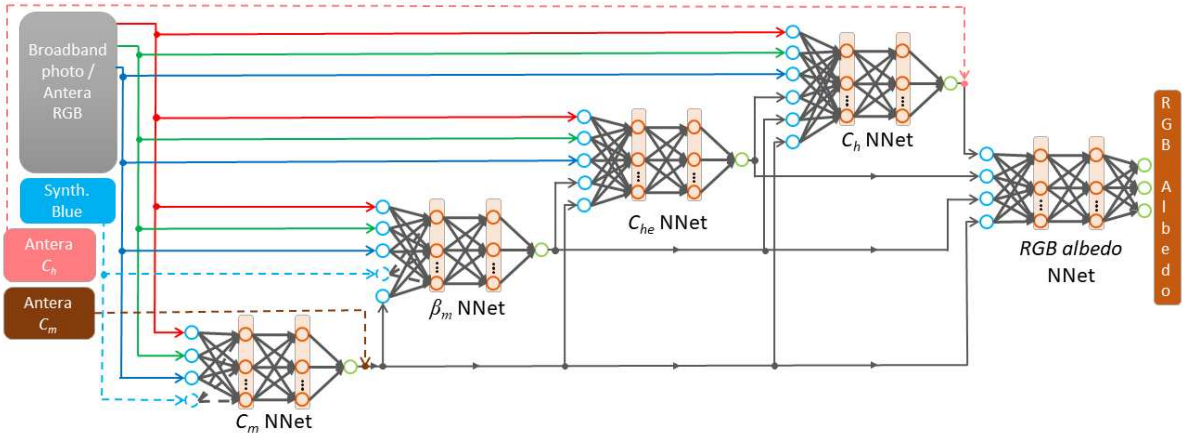

Figure 12: *Pipeline for neural parameter estimation and reconstruction from our measuements.*

2D lookup table (fixed β_m and C_{he}) under the same illumination spectra employed for measuring Antera's albedo map. However, this information of the illumination spectrum for the Antera albedo is not provided by the device or the vendor and, being a proprietary device, we have no control over its LED illumination system in order to make a direct measurement of the appropriate LEDs: the device cycles through all the LEDs very rapidly, making direct measurement of spectrum (e.g., with a spectrometer) difficult. Hence, we estimate the unknown illumination spectrum for the albedo measurement using corresponding measurements of color squares on an Xrite color chart and then solve for the illumination spectrum (see Fig. 11, a) using a genetic algorithm based optmization detailed in Appendix C. We note that the recovered spectrum for Antera's albedo seems to be an approximation of D65 illumination obtained with the LED illuminants on the device. In this respect, it is conceptually very similar to the D65 metamer illumination we create using the LEDs on our LED sphere. Given that we lack the ground truth for Antera's illumination profile, we indirectly validated the spectrum estimation process using a color chart observation under D65 metamer illumination using the LED sphere (see Fig. 11, b).

After recovering the illumination spectrum for Antera's albedo, we can remap Antera's chromophore maps to the appropriate scale using a 2D look-up table based on the reduced Jimenez model. We then fix the C_m and C_h parameters and then re-fit the albedo data to the complete 4D model, this time searching for appropriate values of β_m and C_{he} parameters in a 4D look-up table for fixed values of C_m and C_h. Figure 10 (c) shows reconstruction for the measured cheek patch using this procedure which augments Antera's maps with the two additional parameters required by the 4D model. As can be seen, the reconstruction result of this remapping and augmentation step is a closer match to the albedo map than just remapping the data to the 2D model. We also experimented with directly estimating all four parameters for the model using the albedo map which results in an even closer match for the reconstruction to the measured albedo map (see Figure 10, d). However, the parameter maps estimated using just the albedo map are more noisy and show less physiologically correlated structure than the parameters obtained by remapping and augmenting Antera's maps. This is consistent with our findings in the previous section on practical skin measurements with two complementary spectral illumination conditions. Thus, we believe that parameter maps directly estimated using only the albedo data may be somewhat overfitting to the input data (hence lower reconstruction error) and suffer from some baked-in subsurface scattering visible in the albedo, while the maps estimated by adapting and augmenting Antera's measurements seem to have a higher physiological correlation and hence likely to better generalize to other spectral conditions or for predicting changes in physiological state of skin. We provide additional results for acquired skin patches in Section 7 and Supplemental material.

6. Neural Parameter Estimation

Thus far, we described how to estimate the spectral parameters of skin from our measurements using a look-up table search (for best matching color values in CIELAB space). This process is slow and the results can be prone to image noise and quantization due to discrete values in the look-up table. Hence, instead we also explored a neural prediction approach for obtaining the spectral parameters from our measurements using a cascaded feed-forward multilayer perceptron (MLP) architecture (see Figure 12). We note some conceptual similarity in our approach with that of [YSJR17] who employed MLPs for parameter conversion from one rendering model to another (volumetric scattering to dipole diffusion) for global scattering in hair/fur fibers.

Each of the 4 parameters of our model is estimated by a different MLP (see Fig. 12. From left to right C_mNNET, β_mNNET, $C_{he}NNET$ and C_hNNET), which all share the input from an RGB image, either from our acquisition setup under broadband illumination (D65' or W57) or the albedo map from Antera. In the cascaded order, C_mNNET estimates C_m from the RGB input, and provides the prediction in input to all the subsequent MLPs; similarly, β_mNNET provides its output to $C_{he}NNET$ and C_hNNET, and so on. The last MLP in the cascade sequence, $RGBAlbedoNNET$, takes in input the estimated C_m, β_m, C_{he} and C_h to predict the RGB albedo, ideally matching the input photograph.

To achieve higher accuracy, when the RGB input photograph is provided by our LED sphere setup, C_mNNET and β_mNNET can

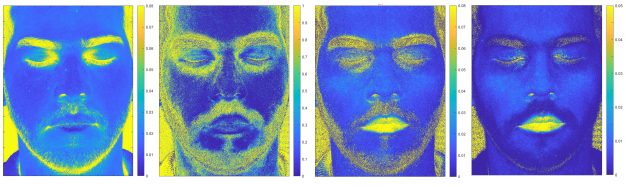

(a) C_m (b) β_m (c) C_h (d) C_{he}

(e) $D65'$ photo (f) $D65'$ recon. (g) $W27$ photo (h) $W27$ recon.

Figure 13: *Spectral parameters for subject's face estimated by the cascaded feed-forward MLP (top-row). The bottom row shows comparison of photographs with reconstructions under D65 metamer broadband illumination (e, f), and warmer W27 LED illumination not employed for parameter estimation (g, h).*

(a) Antera albedo (b) Antera adapted (c) Albedo only

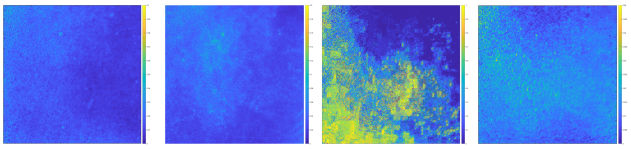

(d) Antera C_m (e) Antera C_h (f) Adapted β_m (g) Adapted C_{he}

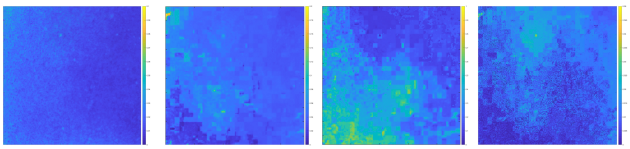

(h) Albedo C_m (i) Albedo C_h (j) Albedo β_m (k) Albedo C_{he}

Figure 14: *Estimating skin patch parameters using the cascaded MLP network on Antera data. Parameters obtained by adapting and augmenting Antera's maps (center row) and from albedo only input (bottom-row). As with the look-up based search, reconstruction with the latter approach is a slightly closer match to the input albedo.*

also take in input the synthesized response to pure blue LED illumination. Additionally, if the RGB input is provided by Antera, its remapped C_m and C_h measurements can be used to bypass respectively C_mNNET and C_hNNET.

6.1. Design and training of the MLPs

The first layer of each MLP is the input layer, followed by two hidden layers (L_1 and L_2) and the output layer. It is well know that two-hidden-layer feedforward networks can approximate complex nonlinear mappings with arbitrary accuracy given enough nodes in the hidden layers and training data. In our pipeline, we train the MLPs on synthetic RGB data, *i.e* the 4D LUTs provided by the spectral skin reflectance model, augmented by zero-mean white gaussian noise to simulate photon shot noise. The noise variance is directly estimated from homogeneous areas in a photograph of a color chart. We then analyze the effect of the noise on the estimated parameters in order to derive a suitable noise model to inject in the skin model parameters used to train the MLPs.

To determine the number of nodes N_{L_1} and N_{L_2} to use in each hidden layer, we observe that the upper bound of the number of nodes per layer can be computed through the following equations [Gua03], where m is the number of output nodes ($m = 1$ for C_mNNET, β_mNNET, $C_{he}NNET$ and C_hNNET, while $m = 3$ for $RGBAlbedoNNET$) and N is the number of distinct training samples (*i.e.* the size of the LUTs):

$$U_{N_{L_1}} = \sqrt{(m+2)N} + 2\sqrt{\frac{N}{m+2}} \tag{2}$$

$$U_{N_{L_2}} = m \cdot \sqrt{\frac{N}{m+2}}. \tag{3}$$

Since such upper bounds might overfit the input data [Gua03], to avoid overfitting and to increase the generalization capabilities of our MLPs we set $N_{L_1} = U_{N_{L_1}}/k$ and $N_{L_2} = U_{N_{L_2}}/k$, with $k \approx 100$, and train the networks using Bayesian regularization backpropagation [Mac92]. Finally, we use a hyperbolic tangent function as activation function.

We train the parameter networks C_mNNET, β_mNNET, $C_{he}NNET$ and C_hNNET once for each input type (e.g., broadband-only or broadband + synth. blue) with $D65'$ as the broadband spectrum for LED sphere data, and the recovered Antera spectrum as the broadband for Antera data. However, the $RGBAlbedoNNET$ used for albedo reconstructions from the input parameters is specific for a given illumination spectrum, and needs to be trained separately for different target illumination spectras.

6.2. Results

Figure 13 presents spectral parameter maps and albedo reconstructions under two uniform spectral illumination conditions, achieved with the above described cascaded MLP network for the subject shown earlier in Figure 7. As can be seen, both the estimated parameters and the RGB albedo reconstructions are very comparable to that achieved using look-up table search, with the added advantage of reduced noise and quantization, as well as significantly faster parameter estimation and reflectance reconstruction (3.5 seconds for MLP network vs 40 minutes with LUT search, i.e., $> 680\times$ speedup for 2K resolution on a laptop with 2.7 GHz Intel Core i7 processor and 16GB RAM) .

Figure 14 demonstrates the cascaded MLP network on the in-

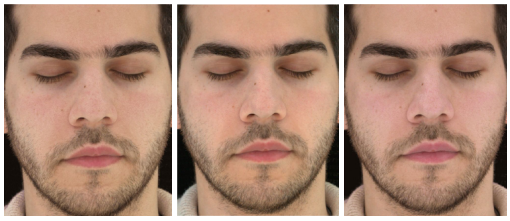

(a) $D65' + blue$ (b) $D65'$ photo (c) $W57 + blue$

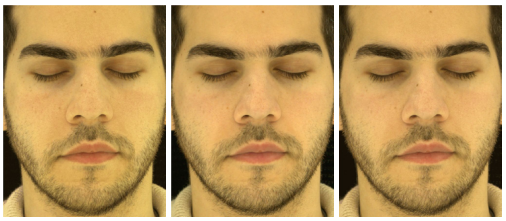

(d) $D65' + blue$ (e) $W57$ photo (f) $W57 + blue$

Figure 15: *Comparison of reconstruction with $D65'$ vs W57 for broadband measurement. Top-row: Reconstructions under $D65'$ illumination compared to photograph (b). Bottom-row: Reconstructions under W57 illumination compared to photograph (e). Left column: Reconstructions with maps estimated with our preferred $D65'$ for broadband illumination. Right column: Reconstructions with maps estimated with W57 (cool white LED) for broadband illumination.*

put provided by Antera on the cheek patch shown earlier in Figure 10, either using its C_m and C_h remapped measurements to bypass C_mNNET and C_hNNET, thus only estimating β_m, C_{he} and albedo (Fig. 14, second row), or directly estimating all four parameters of the model using the albedo map (Fig. 14, third row). As can be seen, the parameters estimated with the MLP network are qualitatively very similar to those obtained with look-up table search shown in Figure 10, with the advantage of much faster estimation. Similar to the look-up table search, estimating the parameters directly from the Antera photograph results in a slightly closer match of the reconstruction to the input albedo map compared to when employing the Antera adapted C_m and C_h parameters.

7. Additional Results and Rendering

We now present additional set of results with our proposed practical spectral measurements for faces, and skin-patch measurements with the Antera3D device. Figure 15 compares the quality of spectral reconstructions with parameters maps estimated when employing our preferred D65 metamer for the broadband measurement (left-colum) vs parameter maps estimated when employing the baseline W57 cool white LED illumination for the broadband measurements (right-column). As can be seen, measurements of the spectral parameters using $D65'$ illumination is able to well predict the appearance under W57. However, when the parameters are estimated using W57 illumination, the predicted appearance under $D65'$ is slightly less accurate, resulting in more saturated colors. This supports our preference for the $D65'$ illumination as the broadband condition for our skin measurements. However, as also shown in Figure 8, our approach still enables parameter estimation of sufficient quality

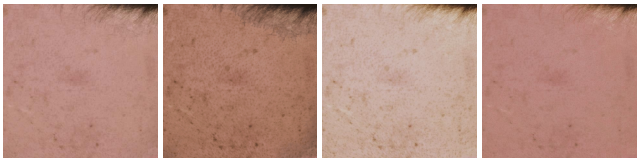

(a) Original (b) Sim. tanning (c) Sim. drained (d) Sim. flushed

Figure 16: *Examples of physiologically based edits to Antera's adapted 4D parameters (a) producing realistic tanning (b), drained (c), and flushed (d) appearance.*

even when employing just two types of LEDs (W57 and blue) for the broadband and narrow-band measurements.

Figure 16 presents examples of physiologically based edits performed on Antera data (a forehead patch). Here, we employ the parameters maps obtained after adapting and augmenting the Antera data to show the original reconstruction of skin appearance (a), followed by simulated tanning (b) by scaling up the C_m parameter by 1.1 in addition to an offset of 0.08 units in cubic root space. Similary we simulate pale drained appearance in (c) by scaling down the original C_h parameter by 1.5 in cubic root space. Finally, flushed skin is simulated in (d) by scaling up the original C_h parameter by 1.1. As can be seen, such simple edits to the adapted Antera maps achieve very realistic physiological changes in skin appearance. We provide a similar example of physiologically based edit for a face in the Supplemental material.

We note that parameters estimated using a single broadband measurement of the albedo encodes some amount of suburface scattering in the parameter maps due to subsurface scattering being baked in the albedo (also observed by Jimenez et al. [JSB*10]). Since our look-up table based reconstruction of the albedo does not do explicit simulations of subsurface scattering, we actually found closer matches (in CIELAB space) to the input photographs when reconstructing the albedo using parameters estimated under a single broadband condition compared to our proposed approach of combining the broadband measurement with narrow-band blue response (also true for Antera data where full 4D search results in better match to input photograph). The reconstructions with our proposed measurements are slightly sharper, with less baked-in subsurface scattering compared to the input photograph which we attribute to the sharp descattered measurement of the narrow-band response. This is actually a desirable outcome for rendering of subsurface scattering with the measured parameter maps. Jimenez et al. employed their measured maps to only reconstruct the albedo which they employed as a modulation texture to a homogeneous subsurface rendering with a fixed diffusion profile. In contrast, our estimated maps allow us to render subsurface scattering with spatially varying albedo and diffusion profiles as explained next.

7.1. Rendering Subsurface Scattering

Inspired by the work of Donner et al. [DWd*08], we employ our estimated parameters to render heterogeneous subsurface scattering in skin. We employed PBRT v2 [PH10] to generate renderings with *pseudo*-heterogeneous subsurface scattering driven by our estimated spatially varying parameters of the spectral BSSRDF model. Given

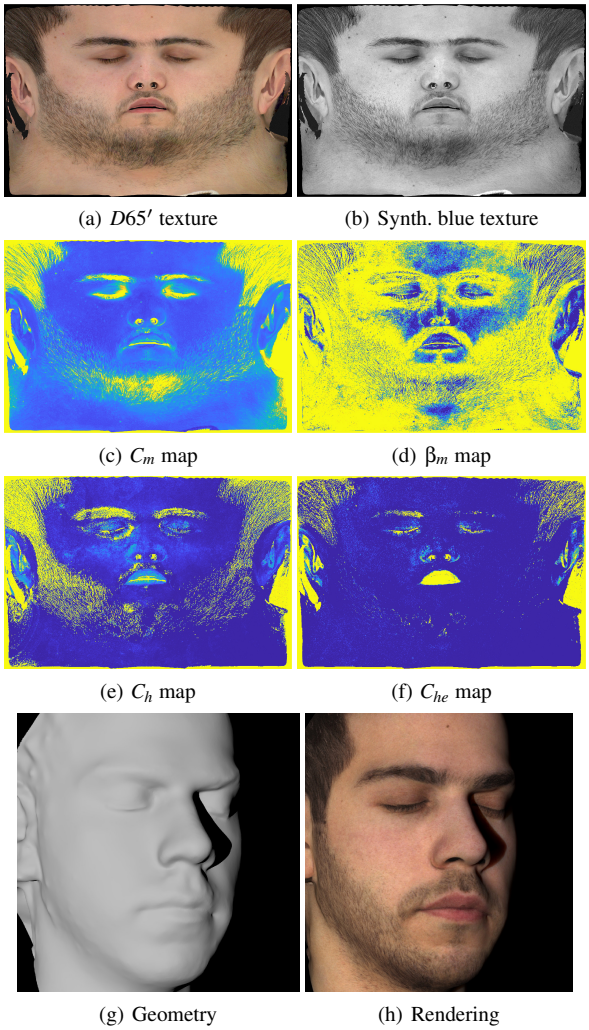

(a) $D65'$ texture (b) Synth. blue texture

(c) C_m map (d) β_m map

(e) C_h map (f) C_{he} map

(g) Geometry (h) Rendering

Figure 17: *$D65'$ and synthesized blue facial textures (a, b), and the estimated chromophore maps (c-f) mapped onto UV texture-space of a face scan. Reconstructed facial geometry (g), and diffuse-only rendering with heterogeneous subsurface scattering (h).*

a facial scan of a subject obtained with multiview acquisition in the LED sphere (we employ COLMAP [SF16, SZPF16] for the base geometry reconstruction), we first project the input data of broadband $D65'$ response (which is also the input to COLMAP for geometry reconstruction) and synthesized narrow-band blue response into the UV texture-space of the face scan (see Figure 17 a, b). We then compute the four spectral parameters of the skin BSSRDF in this UV texture-space and project it onto the base geometry within PBRT for rendering with the skin coloration model.

In order to render heterogeneous subsurface scattering, we modified the provided subsurface scattering implementation in PBRT from the default dipole diffusion kernel to our specified spatially varying profiles implementing two-layered diffusion. For each sampled color generated by the skin model under chosen illumination spectrum, we first pre-compute corresponding spectral reflectance and transmittance profiles for epidermis and dermis separately. We use a dipole model for dermis and a multipole model for epidermis as suggested by [DJ06]. We then convolve these spectral profiles according to Kubelka-Munk formula [DJ05] and store the overall radial reflectance profile function in linear RGB color space. At each point on the surface, PBRT framework extracts the corresponding precomputed spectral reflectance profile from the tabulated set and integrates it over a given radial distance and performs the same operation for all other sampled points on the geometry to add contribution from different spectral profiles, thereby rendering heterogeneous subsurface scattering (more details in Supplemental material). While we convert the spectral profile contributions after integration to RGB within PBRT, it is possible to pre-compute the profiles in sRGB space for usage in a standard RGB rendering pipeline.

Figure 17(h) shows such a diffuse-only rendering of spatially-varying subsurface scattering for a male subject lit with a point light source ($D65'$ spectrum). Figure 1(top-row) presents renderings with additional specular reflectance for the same subject, as well as an additional subject, and a skin patch measured using the Antera camera. Here, we render the specular reflectance as a separate layer in PBRT using a microfacet BRDF with Blinn-Phong distribution, and add it to the diffuse-only rendering as a post-process. We provide additional diffuse-only renderings of the subjects under the illumination spectras of the six types of LEDs in our LED sphere (Figure 1(bottom-row), also see Supplemental material).

Figure 18 presents comparisons of renderings of Subject 1 to photographs under each of the six types of LEDs on the LED sphere. Here, the subject was acquired on a different day compared to the data used for Figure 1(a), with noticable difference in facial hair. As can be seen, renderings with the estimated parameters correctly predict the change in appearance across the six spectrums, with characteristic softening of skin texture under the warmer spectrums. We additionally provide qualitative comparisons (against photographs) of renderings with parameters estimated using our proposed two complementary measurements vs using a single broadband measurement for parameter estimation (which results in softer, blurry skin appearance) in the Supplemental material.

Note that the facial geometry and spectral measurements for the face renderings were acquired using a multiview capture setup (9 DSLR cameras) placed around the LED sphere. For rendering subsurface scattering in PBRT v2, we had to significantly downsample the mesh vertices, thereby rendering a smooth base mesh seen in Figure 17. For rendering the specular layer in Figure 1, we compute shading based on a photometric normal map acquired using the LED sphere. The geometry for the back of the hand in Figure 1 is provided by the Antera software which computes the shape of a relatively planar skin patch using photometric stereo which we directly employ for both the subsurface and specular rendering.

7.2. Limitations and Discussion

The employed 4D skin BSSRDF model is well suited to reconstruct the appearance of skin and facial hair but has limitations and cannot well reconstruct the appearance of domiant veins or tattoos in skin (see Supplemental material). This is because veins and tattoos cannot be modeled with melanin and hemoglobin concentrations [DWd*08]. We currently do not model any fluorescence in skin, although our

(a) W57 (b) W40 (c) W27 (d) Red (e) Green (f) Blue

Figure 18: *Comparison of photographs of subject lit with cross-polarized point light source with 6 different LED spectras (top-row), against renderings driven by spectral parameters estimated using two complementary measurements (bottom-row).*

broadband measurements likely include some effects of dermal fluorescence [GZAK00]. Through our analysis, we show that parameter estimation using just a single broadband illumination is possible, although suboptimal. The quality and structural physiological correlation of the estimated parameters increases with multiple measurements. In this respect, our proposed two shot acquisition with the complementary spectral illumination conditions is a practical middle ground between the highly accurate measurements possible with detailed spectral imaging as demonstrated by [DWd*08] (also employed by the Antera camera), and just single broadband illumination previously employed for practical measurements of faces. Our choice of illuminants is also a function of the LEDs available in our facial capture setup, and the optimal choices may vary slightly for other spectral illumination setups. However, we demonstrate through our analysis the general trend of the desired illumination conditions for skin measurements, and a method for approximating desirable D65 spectrum using combination of available LEDs. Note that an LED sphere is not a strict requirement for the measurements since the method only requires uniform illumination, and hence can be adapted for many facial capture setups. When employing the Antera camera, we are rather restricted to only using the processed outputs of its proprietary software which does not allow access to the raw data of the spectral measurements for further analysis. However, we demonstrate how to adapt black-box measurements from such a custom dermatological scanning device for realistic rendering.

For the LED sphere measurements, we currently estimate parameters assuming uniform illumination with no occlusions. However, for faces there is partial ambient occlusion around eye sockets and the nose that is baked into the measurements and by extension in our estimated parameter maps. We also do not currently explicitly account for the effect of exitant Frensel in these measurements which slightly affects the parameters estimated for surfaces seen at a grazing angle (most visible in the β_m map). This is not really a problem for our 3D renderings which employ data seen from 9 different viewpoints and hence the facial parameter maps in the UV parameterization of the geometry is composed of mostly near normal incidence estimates. Finally, our look-up table based reconstructions reproduce the coloration of albedo texture under uniform illumination, but do not model lateral scattering of light within skin which requires explicit rendering of subsurface scattering.

8. Conclusion

In summary, we have presented novel practical spectral measurements of skin reflectance using both a dedicated spectral illumination setup (LED sphere) and an off-the-shelf skin measurement device (Antera3D), and employed them to drive a spectral skin BSSRDF model with appropriate complexity to match the appearance of real skin. In this respect, our main contribution is proposing a sweet spot both for measurement and data-driven modeling complexity for reproducing the appearance of skin, including human faces. Our additional contributions include investigating desirable illumination spectra realizable with common LEDs, practical analysis of the gamut limitations of regular RGB color cameras for measuring response to narrow band LED illumination, and proposing a novel indirect measurement protocol that overcomes the gamut limitation and achieves improved spectral isolation compared to direct measurement with a color camera. We also demonstrate how to adapt practical hand-held physiological measurements from a dermatological skin measurement device to our application of realistic rendering which can have a significant impact for dermatological visualizations. Additionally, we also demonstrate how neural networks can be employed for much more efficient parameter estimation and spectral reconstructions given various types of measurements. We see this as a promising initial step towards efficient machine-learning based spectral skin rendering and diagnostics. We demonstrate highly realistic reconstructions of skin with our approach, including renderings of human faces using a biophysically based skin BSSRDF that are, for the *first* time, comparable to photographs. Future work in this direction could investigate practical measurements and modeling of changes in skin parameters due to skin dynamics or physiological factors of interest for medical diagnostics, as well as applications of any skin products.

9. Acknowledgements

We thank our annonymous reviewers for their valuable feedback, and Yiming Lin, Antoine Toisoul and Jolande Fooken for agreeing to be measurement subjects. This work was supported by an EPSRC Early Career Fellowship (EP/N006259/1), and by the Spectraskin project N-288670, funded by the Research Council of Norway.

References

[AS17] ALOTAIBI S., SMITH W. A. P.: A biophysical 3d morphable model of face appearance. In *2017 IEEE International Conference on Computer Vision Workshops, ICCV Workshops 2017, Venice, Italy, October 22-29, 2017* (2017), pp. 824–832. 3

[BCF01] BARNARD K., CIUREA F., FUNT B.: Sensor sharpening for computational color constancy. *Journal of the Optical Society of America. A, Optics, image science, and vision 18* (12 2001), 2728–43. 3

[BS10a] BIANCO S., SCHETTINI R.: Two new von kries based chromatic adaptation transforms found by numerical optimization. *Color Research & Application 35*, 3 (2010), 184–192. 15

[BS10b] BRAINARD D. H., STOCKMAN A.: Colorimetry. McGraw Hill, 2010. 15

[CBKM15] CHEN T. F., BARANOSKI G. V. G., KIMMEL B. W., MIRANDA E.: Hyperspectral modeling of skin appearance. *ACM Trans. Graph. 34*, 3 (May 2015), 31:1–31:14. 2, 3

[CCH99] COTTON S. D., CLARIDGE E., HALL P. N.: A skin imaging method based on a colour formation model and its application to the diagnosis of pigmented skin lesions. In *Proceedings of Medical Image Understanding and Analysis '99* (1999), pp. 49–52. 3

[CXW19] CHAUHAN T., XIAO K., WUERGER S.: Chromatic and luminance sensitivity for skin and skinlike textures. *Journal of Vision 19*, 1 (2019). 5

[DJ05] DONNER C., JENSEN H. W.: Light diffusion in multi-layered translucent materials. *ACM Transactions on Graphics (TOG) 24*, 3 (2005), 1032–1039. 2, 11

[DJ06] DONNER C., JENSEN H. W.: A spectral bssrdf for shading human skin. In *Proceedings of the 17th Eurographics Conference on Rendering Techniques* (Aire-la-Ville, Switzerland, Switzerland, 2006), EGSR '06, Eurographics Association, pp. 409–417. 2, 11

[DWd*08] DONNER C., WEYRICH T., D'EON E., RAMAMOORTHI R., RUSINKIEWICZ S.: A layered, heterogeneous reflectance model for acquiring and rendering human skin. *ACM Transactions on Graphics (TOG) 27*, 5 (Dec. 2008), 140:1–140:12. 2, 3, 10, 11, 12

[GFT*11] GHOSH A., FYFFE G., TUNWATTANAPONG B., BUSCH J., YU X., DEBEVEC P.: Multiview face capture using polarized spherical gradient illumination. *ACM Transactions on Graphics (TOG) 30*, 6 (2011), 129. 4

[GHP*08] GHOSH A., HAWKINS T., PEERS P., FREDERIKSEN S., DEBEVEC P.: Practical modeling and acquisition of layered facial reflectance. *ACM Trans. Graph. 27*, 5 (Dec. 2008), 139:1–139:10. 2

[Gua03] GUANG-BIN HUANG: Learning capability and storage capacity of two-hidden-layer feedforward networks. *IEEE Transactions on Neural Networks 14*, 2 (March 2003), 274–281. 9

[GZAK00] GILLIES R., ZONIOS G., ANDERSON R., KOLLIAS N.: Fluorescence excitation spectroscopy provides information about human skin in vivo. *Journal of Investigative Dermatology 115*, 4 (2000). 12

[IGAJG15] IGLESIAS-GUITIAN J. A., ALIAGA C., JARABO A., GUTIERREZ D.: A biophysically-based model of the optical properties of skin aging. *Comput. Graph. Forum 34*, 2 (May 2015), 45–55. 2, 3

[INN07] IGARASHI T., NISHINO K., NAYAR S. K.: The appearance of human skin: A survey. *Found. Trends. Comput. Graph. Vis. 3*, 1 (Jan. 2007), 1–95. 2

[JMLH01] JENSEN H. W., MARSCHNER S., LEVOY M., HANRAHAN P.: A practical model for subsurface light transport. In *In Proceedings of ACM SIGGRAPH* (2001), pp. 511–518. 2

[JSB*10] JIMENEZ J., SCULLY T., BARBOSA N., DONNER C., ALVAREZ X., VIEIRA T., MATTS P., ORVALHO V., GUTIERREZ D., WEYRICH T.: A practical appearance model for dynamic facial color. *ACM Transactions on Graphics (TOG) 29*, 6 (Dec. 2010), 141:1–141:10. 2, 3, 4, 10

[JSG09] JIMENEZ J., SUNDSTEDT V., GUTIERREZ D.: Screen-space perceptual rendering of human skin. *ACM Transactions on Applied Perception 6*, 4 (2009), 23:1–23:15. 3

[KB04] KRISHNASWAMY A., BARANOSKI G. V. G.: A biophysically-based spectral model of light interaction with human skin. *Comput. Graph. Forum 23* (2004), 331–340. 3

[KRP*15] KLEHM O., ROUSSELLE F., PAPAS M., BRADLEY D., HERY C., BICKEL B., JAROSZ W., BEELER T.: Recent advances in facial appearance capture. *Computer Graphics Forum (CGF) 34*, 2 (May 2015), 709–733. 2

[LWA*18] LINMING F., WEI H., ANQI L., YUANYU C., HENG X., SUSHMITA P., YIMING L., LI L.: Comparison of two skin imaging analysis instruments: The visia from canfield vs the antera 3d cs from miravex. *Skin Research and Technology 24*, 1 (2018), 3–8. 7

[LYL*16] LEGENDRE C., YU X., LIU D., BUSCH J., JONES A., PATTANAIK S., DEBEVEC P.: Practical multispectral lighting reproduction. *ACM Trans. Graph. 35*, 4 (July 2016), 32:1–32:11. 3, 14

[Mac92] MACKAY D. J. C.: Bayesian interpolation. *Neural Computation 4*, 3 (1992), 415–447. 9

[MFCN15] MATIAS A. R., FERREIRA M., COSTA P., NETO P.: Skin colour, skin redness and melanin biometric measurements: comparison study between antera 3d, mexameter and colorimeter. *Skin Research and Technology 21*, 3 (2015), 346–362. 7

[PC04] PREECE S., CLARIDGE E.: Spectral filter optimization for the recovery of parameters which describe human skin. *IEEE Transactions on Pattern Analysis and Machine Intelligence 26*, 7 (2004), 913 – 922. 3, 5

[PH10] PHARR M., HUMPHREYS G.: *Physically Based Rendering: From Theory to Implementation*. Morgan Kaufman, 2010. 10

[PLGN07] PARK J., LEE M., GROSSBERG M. D., NAYAR S. K.: Multispectral imaging using multiplexed illumination. In *Proceedings of IEEE International Conference on Computer Vision (ICCV)* (2007). 3

[SF16] SCHÖNBERGER J. L., FRAHM J.-M.: Structure-from-motion revisited. In *Conference on Computer Vision and Pattern Recognition (CVPR)* (2016). 11

[SZPF16] SCHÖNBERGER J. L., ZHENG E., POLLEFEYS M., FRAHM J.-M.: Pixelwise view selection for unstructured multi-view stereo. In *European Conference on Computer Vision (ECCV)* (2016). 11

[TOS*03] TSUMURA N., OJIMA N., SATO K., SHIRAISHI M., SHIMIZU H., NABESHIMA H., AKAZAKI S., HORI K., MIYAKE Y.: Image-based skin color and texture analysis/synthesis by extracting hemoglobin and melanin information in the skin. *ACM Trans. Graph. 22*, 3 (July 2003). 3

[Tuc07] TUCHIN V.: *Tissue Optics: Light Scattering Methods and Instruments for Medical Diagnosis*, vol. PM166. The International Society for Optics and Photonics (SPIE), 2007. 2

[WHD03] WENGER A., HAWKINS T., DEBEVEC P.: Optimizing color matching in a lighting reproduction system for complex subject and illuminant spectra. In *Proceedings of the 14th Eurographics Workshop on Rendering* (2003), EGRW '03, pp. 249–259. 3

[WLL*09] WEYRICH T., LAWRENCE J., LENSCH H. P. A., RUSINKIEWICZ S., ZICKLER T.: Principles of appearance acquisition and representation. *Found. Trends. Comput. Graph. Vis. 4*, 2 (Feb. 2009), 75–191. 2

[WMP*06] WEYRICH T., MATUSIK W., PFISTER H., BICKEL B., DONNER C., TU C., MCANDLESS J., LEE J., NGAN A., JENSEN H. W.,

GROSS M.: Analysis of human faces using a measurement-based skin reflectance model. *ACM Transactions on Graphics (TOG) 25*, 3 (July 2006), 1013–1024. 2

[WS82] WYSZECKI G., STILES W. S.: *Color science: Concepts and Methods, Quantitative Data and Formulae*, vol. 8. Wiley, New York, NY, USA, 1982. 14

[YSJR17] YAN L.-Q., SUN W., JENSEN H. W., RAMAMOORTHI R.: A bssrdf model for efficient rendering of fur with global illumination. *ACM Trans. Graph. 36*, 6 (Nov. 2017). 8

Appendix A: D65 Metamer

We address the problem of reproducing a desired spectral illumination (D65) using the LEDs in our LED sphere relying on the faithful reproduction of the appearance of a color chart. We first acquire a set of images of the color chart with known reflectance, individually under each of the $n = 6$ LEDs. The measurements are taken at 3 different LED intensities, under uniform spherical illumination. Given the knowledge of the camera spectral sensitivity *CSS*, measured with a monochromator, this data allows us to recover the per-channel (ch) non-linear response of the camera sensor γ_{ch}, and the LEDs relative intensities α_k.

This is similar to the approach of LeGendre et al. [LYL*16], except that instead of focusing only on the color chart appearance to a given camera, we also aim at maximizing the faithfulness of perceived color appearance to a human observer. The reason for simultaneously accounting for a percetual metric besides camera sensitivity in our optimization is that the Chromatic Adaptation Transform (Appendix B) employed for spectral isolation of narrowband response, and look-up table search for the spectral parameters are all based on perceptual metrics. In order to find a spectrum which satisfies the above, given the weights w_c and w_h for the camera and perceptual terms respectively, we need to find a set of coefficients ${\alpha^*}_k$, for the $n = 6$ LEDs which minimizes the following equation:

$$w_c t_c + w_h t_h \tag{4}$$

$$t_c = \sum_{j=1}^{N_p} \sum_{ch=r,g,b} \left\| DG_{j,ch} - \left(\sum_{k=1}^{n} {\alpha'}_k \sum_{\lambda=380}^{720} CSS_{ch,\lambda} S_{k,\lambda} R_{j,\lambda} \right)^{\gamma_{ch}} \right\| \tag{5}$$

$$t_h = \frac{1}{N_p} \sum_{j=1}^{N_p} \Delta E_{2k} \left(Lab_{D65,j}, XYZ \rightarrow Lab \left(\left[X_{j,{\alpha'}_k}, Y_{j,{\alpha'}_k}, Z_{j,{\alpha'}_k} \right] \right) \right); \tag{6}$$

where DLj,ch are the per-channel digital levels of the patch j of the color chart, $Lab_{D65,j}$ are the CIELab values of the color chart patches under D65 illumination, $XYZ \rightarrow Lab$ is a standard conversion using the D65 reference white [WS82], and $\left[X_{j,{\alpha'}_k}, Y_{j,{\alpha'}_k}, Z_{j,{\alpha'}_k}\right]$ are the XYZ tristimulus values of the color chart patches under the spectrum resulting from the coefficient ${\alpha'}_k$, computed using the $\hat{x}, \hat{y}, \hat{z}$ CIE 2° colour matching functions. The coefficients ${\alpha^*}_k$ are found by means of a convex non-linear optimization, constraining the solution to have all non negative values.

Figure 19(a) shows the quality of the D65 *metamer* found by means of the above optimization, by comparing the color chart appearance under the ideal D65 spectrum (background of each square), and the appearance of the color chart under the metamer shown in the circles at the center of each square (mostly barely visible or invisible). Given that this solution for the D65 metamer requires our specific set of 6 LEDs which may not be common, we repeated the experiment by using the Red, Green, and Blue LEDs along with only one of the broadband white LEDs at a time since an RGBW lighting system might be more common. The results, reported in Fig. 19 (b)-(d), show that the overall color rendition quality of the system is somewhat reduced. However, a very reasonable approximation of the D65 can be still found by using the W57 cool white LED in combination with RGB LEDs which is consistent with the findings of [LYL*16].

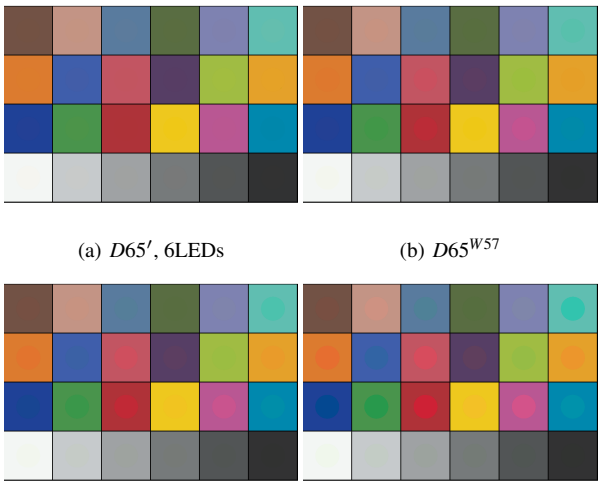

(a) $D65'$, 6LEDs (b) $D65^{W57}$

(c) $D65^{W40}$ (d) $D65^{W27}$

Figure 19: *Quality of D65 metamers created by various combination of LEDs on the LED sphere. (a) Ideal metamer created when combining all 6 LEDs. (b) Employing only cool white LED (W57) in combination with the RGB LEDs also achieves a decent quality metamer. The quality drops off when combining RGB LEDs with one of the warmer white LEDs (c, d).*

Appendix B: Chromatic Adaptation Transform

The Chromatic Adaptation Transform (CAT) of an image $CAT\,(I_{Ill})$ is computed in the CIE XYZ tristimulus values space, where its predicted $[X^{D65} Y^{D65} Z^{D65}]^T$ values under D65 illumination are derived as follows:

$$\begin{bmatrix} X^{D65} \\ Y^{D65} \\ Z^{D65} \end{bmatrix} = M_{CAT} * \begin{bmatrix} \alpha^{D65}/\alpha^{Ill} & & \\ & \beta^{D65}/\beta^{Ill} & \\ & & \gamma^{D65}/\gamma^{Ill} \end{bmatrix} * M_{CAT} * \begin{bmatrix} X^{Ill} \\ Y^{Ill} \\ Z^{Ill} \end{bmatrix}, \tag{7}$$

where

$$\begin{bmatrix} \alpha^{D65} \\ \beta^{D65} \\ \gamma^{D65} \end{bmatrix} = M_{CAT} * \begin{bmatrix} {X_w}^{D65} \\ {Y_w}^{D65} \\ {Z_w}^{D65} \end{bmatrix} \tag{8}$$

and

$$\begin{bmatrix} \alpha^{Ill} \\ \beta^{Ill} \\ \gamma^{Ill} \end{bmatrix} = M_{CAT} * \begin{bmatrix} {X_w}^{Ill} \\ {Y_w}^{Ill} \\ {Z_w}^{Ill} \end{bmatrix}. \tag{9}$$

In the above, $[{X_w}^{Ill} {Y_w}^{Ill} {Z_w}^{Ill}]^T$ and $[{X_w}^{D65} {Y_w}^{D65} {Z_w}^{D65}]^T$ respectively represent the tristimulus values of the source *Ill* and *D*65 illuminants. The 3×3 matrix M_{CAT} models human color perception at the LMS cone response level [BS10b], and is derived by numerical optimization [BS10a]. Please note that, given the typical overlapping design of camera sensors spectral sensitivity, the red and green channels of I_{nb} might contain non-zero signal, similarly to a direct acquisition of a photograph under narrow band illumination.

Appendix C: Estimating Antera's LED spectrum

The lack of control over Antera's LEDs, both in terms of switching sequence and speed, makes it difficult to directly measure the lighting spectra using a spectrometer given the typical integration time of over 1 second per measurement. Moreover, the individual LEDs have different orientations, thus requiring an integrating sphere for accurate spectral measurements. Hence, we opted for spectral recovery by means of a Genetic Algorithm (GA) based optimization by providing as input to our algorithm a sequence of photographs of a standard reference colour chart, with $N_p = 24$ colour patches of known spectral reflectance R.

Our GA begins with a random guess for the Antera's LEDs spectra S: the optimization is driven by a fitness function f, which measures the differences between the acquired digital levels and the simulated ones according to a standard camera model:

$$f(S,CSS) = \sum_{n=1}^{N_p} \sum_{ch=r,g,b} \left\| DG_{n,ch} - \left(\sum_{\lambda=380}^{720} CSS_{ch,\lambda} \cdot S_\lambda \cdot R_{n,\lambda} \right)^{\gamma_{ch}} \right\|, \tag{10}$$

where $DG_{n,ch}$ is the acquired digital level of the *ch* channel of the colour patch n and γ_{ch} models the per-channel non-linear response of the sensor.

The above equation implies the joint estimation of the incident spectra S and the Antera's spectral sensitivity *CSS*. Hence, a naïve implementation would be extremely underconstrained. However, the specifications of the Antera camera report that it can be used as a colorimeter, thus implying that the spectral sensitivity must fulfill Luther's condition (*i.e.* it is a linear transformation of the CIE 1931 2-degree Colour Matching Functions), greatly reducing the search space. Furthermore, we enforce the recovery of the LEDs spectra by augmenting $f(S,CSS)$ with a smoothness constraint:

$$f'(S,CSS) = f(S,CSS) \cdot (1 + \left\| \frac{\sigma(\delta(S))}{\overline{\delta(S)}} \right\| / k), \tag{11}$$

where K is a scale constant related to the desired resolution in *nm* of S and *CSS*; σ and δ respectively indicates standard deviation and derivative. Figure 11 reports the recovered overall spectrum of the illumination employed for Antera's albedo measurement. Note that the various peaks correspond to the various types of narrow band LEDs on the device, and the intensity of the recovered peaks might be affected by the different orientations of the LEDs.